

Transverse Charge Density and the Radius of the Proton

Alexander V. Gramolin¹ and Rebecca L. Russell²

¹*Department of Physics, Boston University, Boston, Massachusetts 02215, USA*

²*The Charles Stark Draper Laboratory, Inc., Cambridge, Massachusetts 02139, USA*

A puzzling discrepancy exists between the values of the proton charge radius obtained using different experimental techniques: elastic electron-proton scattering and spectroscopy of electronic and muonic hydrogen. The proton radius is defined through the slope of the electric form factor, $G_E(Q^2)$, at zero four-momentum transfer, which is inaccessible in scattering experiments. We propose a novel method for extracting the proton radius from scattering data over a broad Q^2 range rather than attempting to directly determine the slope of G_E at $Q^2 = 0$. This method relates the radius of the proton to its transverse charge density, which is the two-dimensional Fourier transform of the Dirac form factor, $F_1(Q^2)$. We apply our method to reanalyze the extensive data obtained by the A1 Collaboration [J. C. Bernauer *et al.*, *Phys. Rev. Lett.* **105**, 242001 (2010)] and extract a radius value, $r_E = 0.889(5)_{\text{stat}}(5)_{\text{syst}}(4)_{\text{model}}$ fm, that is consistent with the original result. We also provide new parametrizations for the Dirac and Pauli form factors and the transverse charge and magnetization densities of the proton. Our reanalysis shows that the proton radius discrepancy cannot be explained by issues with fitting and extrapolating the A1 data to $Q^2 = 0$.

Introduction. Over a century after Rutherford’s discovery of the proton [1], some fundamental properties of this particle are still not well understood. In particular, the proton charge radius, r_E , remains experimentally puzzling. Beginning with the pioneering research [2, 3], r_E has long been measured in elastic electron-proton scattering experiments [4–10]. It has also been extracted from atomic transition frequencies in both electronic [11–15] and muonic [16, 17] hydrogen. The 2014 CODATA recommended value of r_E , obtained from all non-muonic data available at the time, is 0.8751(61) fm [11]. In contrast, muonic hydrogen spectroscopy yielded the value $r_E = 0.84087(39)$ fm [17], which is smaller by 5.6 standard deviations. More recently, there have been experimental results in favor of both the smaller [10, 12, 14, 15] and larger [9, 13] values of the proton radius. The striking discrepancy between different measurements of r_E has become known as the “proton radius puzzle” [18–20]. In this Letter, we propose a novel method for extracting r_E from scattering data and use it to reanalyze the measurement reported in Refs. [5, 6].

The electromagnetic structure of the proton is encoded in its Dirac and Pauli form factors, $F_1(Q^2)$ and $F_2(Q^2)$, which depend on the negative four-momentum transfer squared, $Q^2 = -q^2$ (see textbooks [21–23]). Instead of F_1 and F_2 , it is often more convenient to use the Sachs electric and magnetic form factors, defined as

$$G_E = F_1 - \frac{Q^2}{4M^2}\kappa F_2, \quad G_M = F_1 + \kappa F_2, \quad (1)$$

where $M \approx 0.938$ GeV is the mass of the proton and $\kappa \approx 1.793$ is its anomalous magnetic moment. The Sachs form factors have a simple interpretation when considered in the Breit frame, where the exchanged virtual photon carries momentum \mathbf{q} but no energy [21–23]. In this frame, $Q^2 = \mathbf{q}^2$ and G_E and G_M can be interpreted as the three-dimensional Fourier transforms of the proton’s spatial charge and magnetization densities, respectively.

Unfortunately, the concept of the three-dimensional densities is valid only in the non-relativistic limit, when $Q^2 \ll M^2$ and the Breit frame coincides with the proton rest frame [21, 24, 25]. For this reason, the proton radius cannot be properly determined through the three-dimensional charge density and is instead defined as

$$r_E = \sqrt{-6 \left. \frac{dG_E(Q^2)}{dQ^2} \right|_{Q^2=0}} \quad (2)$$

in both scattering and spectroscopic measurements [24]. However, the definition (2) is inconvenient for scattering experiments: it requires measuring G_E at the lowest achievable Q^2 values, extrapolating the data down to $Q^2 = 0$, and then inferring the slope of G_E at that point. Such a procedure is inevitably model dependent, which greatly complicates the extraction of the proton radius [26–31]. We propose to avoid these issues by relating the radius of the proton to its transverse charge density, which has a proper relativistic interpretation and can be determined from scattering data over a broad Q^2 range.

Transverse charge density. In this section, we briefly review the definition of the transverse charge density and its relation to the proton radius [24, 25, 32–39]. We start with a change of space-time coordinates from the usual (x^0, x^1, x^2, x^3) to (x^+, x^-, \mathbf{b}) , where $x^\pm = (x^0 \pm x^3)/\sqrt{2}$ are the light-cone variables and $\mathbf{b} = (x^1, x^2)$ is the transverse position vector. By setting $q^+ = 0$, we specify the infinite-momentum frame in which q^μ has only transverse components: $q^\mu = (0, 0, \mathbf{q}_\perp)$ and $Q^2 = \mathbf{q}_\perp^2$. Then, the Dirac form factor $F_1(Q^2)$ can be related to a circularly-symmetric transverse charge density of the proton, $\rho_1(b)$, by the following two-dimensional Fourier transforms:

$$F_1(Q^2) = 2\pi \int_0^\infty b \rho_1(b) J_0(Qb) db, \quad (3)$$

$$\rho_1(b) = \frac{1}{2\pi} \int_0^\infty Q F_1(Q^2) J_0(Qb) dQ, \quad (4)$$

where $b = |\mathbf{b}|$ is the impact parameter and J_0 denotes the Bessel function of the first kind of order zero. As the forward and inverse Fourier transforms, Eqs. (3) and (4) are dual representations of the same quantity in momentum and position spaces. For example, the m -pole form factor,

$$F_{m\text{-pole}}(Q^2) = \left(1 + \frac{Q^2}{\Lambda^2}\right)^{-m}, \quad (5)$$

which is a generalization of the monopole ($m = 1$) and dipole ($m = 2$) form factors, corresponds to

$$\rho_{m\text{-pole}}(b) = \frac{\Lambda^{m+1} b^{m-1}}{2^m (m-1)! \pi} K_{m-1}(\Lambda b), \quad (6)$$

where Λ is a scale parameter and K_{m-1} denotes the modified Bessel function of the second kind of order $m-1$. Note that $\rho_1(b)$ has a proper density interpretation even in the relativistic case [24]. As a reduction of the generalized parton distributions, it can be related to observables in deep inelastic scattering [34].

Expanding $J_0(Qb)$, we can rewrite Eq. (3) as

$$F_1(Q^2) = 1 - \frac{\langle b_1^2 \rangle}{4} Q^2 + \frac{\langle b_1^4 \rangle}{64} Q^4 - \dots, \quad (7)$$

where

$$\langle b_1^n \rangle = 2\pi \int_0^\infty b^{n+1} \rho_1(b) db \quad (8)$$

is the n -th moment of $\rho_1(b)$ and $F_1(0) = \langle b_1^0 \rangle = 1$. The moment expansion (7) indicates that the mean-square transverse charge radius of the proton is

$$\langle b_1^2 \rangle = -4 \left. \frac{dF_1(Q^2)}{dQ^2} \right|_{Q^2=0}. \quad (9)$$

Equation (9) is analogous to the proton radius definition (2). Note that Eqs. (8) and (9) are not equivalent: any fit of the experimental data obtained at $Q^2 > 0$ predicts some slope for F_1 at $Q^2 = 0$ but does not necessarily correspond to a finite transverse charge density. For example, the Fourier integral (4) diverges if F_1 is a polynomial in Q^2 . Therefore, Eqs. (4) and (8) impose additional physical constraints on the fit that is used to extract $\langle b_1^2 \rangle$.

It is important to recognize that there is a simple connection between r_E and $\langle b_1^2 \rangle$. Indeed, after differentiating Eq. (1) for G_E with respect to Q^2 , setting $Q^2 = 0$, and substituting Eqs. (2) and (9), we obtain

$$r_E = \sqrt{\frac{3}{2} \left(\langle b_1^2 \rangle + \frac{\kappa}{M^2} \right)}. \quad (10)$$

This equation defines the proton radius through the second moment (8) of the transverse charge density. Note that we use Eq. (9) only to derive the relation (10) but not to experimentally determine $\langle b_1^2 \rangle$.

Parametrizations for $\rho_1(b)$ and $F_1(Q^2)$. In principle, one can use Eq. (4) to determine $\rho_1(b)$ directly from the experimental data for $F_1(Q^2)$, then calculate $\langle b_1^2 \rangle$ according to Eq. (8), and finally obtain the proton radius using Eq. (10). In practice, it is easier to parametrize $F_1(Q^2)$ and $\rho_1(b)$ such that both the Fourier transforms (3) and (4), as well as the moments (8), can be calculated analytically. Since $F_1(Q^2)$ at small Q^2 is close to the dipole form factor, we expect that $\rho_1(b)$ can be approximated as $\rho_{2\text{-pole}}(b)$ times a polynomial in Λb . Particularly suitable are the orthogonal polynomials $P_n^{(\nu)}$ defined by the orthonormality condition

$$\int_0^\infty P_m^{(\nu)}(x) P_n^{(\nu)}(x) w_\nu(x) dx = \delta_{mn}, \quad (11)$$

where

$$w_\nu(x) = \frac{2}{\Gamma(\nu+1)} x^{\nu/2} K_\nu(2\sqrt{x}) \quad (12)$$

is the weight function, m and n are the degrees of the polynomials, δ_{mn} is the Kronecker delta, and Γ denotes the gamma function. These polynomials have recently been studied in Ref. [40] (note that we use a different normalization for the weight function). We choose $\nu = 1$ and $x = \Lambda^2 b^2/4$ to match $w_\nu(x)$ with $\rho_{2\text{-pole}}(b)$. The first three corresponding polynomials are

$$P_0^{(1)}(x) = 1, \quad P_1^{(1)}(x) = \frac{x-2}{2\sqrt{2}}, \quad (13)$$

$$P_2^{(1)}(x) = \frac{x^2 - 15x + 18}{6\sqrt{26}}. \quad (14)$$

For more terms, see Supplemental Material [41].

We can therefore approximate the transverse charge density as a truncated series

$$\rho_1(b) \approx \rho_{2\text{-pole}}(b) \sum_{n=0}^N \alpha_n P_n^{(1)}(\Lambda^2 b^2/4), \quad (15)$$

where α_n are the expansion coefficients. After substituting Eq. (15) into Eq. (8), we find

$$\langle b_1^0 \rangle = \alpha_0, \quad \langle b_1^2 \rangle = \frac{8}{\Lambda^2} (\alpha_0 + \sqrt{2}\alpha_1). \quad (16)$$

In general, $\langle b_1^{2n} \rangle$ is a linear combination of $\alpha_0, \alpha_1, \dots, \alpha_n$. Therefore, if Λ is fixed, there is a one-to-one correspondence between the expansion coefficients α_n and the even moments of the transverse charge density (15).

After substituting the series expansion (15) into Eq. (3), we obtain the following parametrization for the

Dirac form factor:

$$F_1(Q^2) \approx \sum_{n=0}^N \alpha_n A_n(Q^2/\Lambda^2), \quad (17)$$

where

$$A_0(y) = \frac{1}{(1+y)^2}, \quad (18)$$

$$A_1(y) = -\frac{y(y+4)}{\sqrt{2}(1+y)^4}, \quad (19)$$

$$A_2(y) = \frac{y^2(3y^2+22y+39)}{\sqrt{26}(1+y)^6}, \dots, \quad (20)$$

$$A_N(y) = \int_0^\infty P_N^{(1)}(x) w_1(x) J_0(2\sqrt{xy}) dx \quad (21)$$

are rational functions.

Extending our formalism to the Pauli form factor, we can represent it as

$$F_2(Q^2) = 2\pi \int_0^\infty b \rho_2(b) J_0(Qb) db, \quad (22)$$

where $\rho_2(b)$ is the transverse magnetization density [42]. It is argued in Ref. [37] that $\rho_M = -b(d\rho_2/db)$ is a better defined quantity. (There is also a closely-related transverse charge density of a polarized proton [25, 36].) However, we are not concerned here with the physical interpretation of $\rho_2(b)$ and use it only to parametrize $F_2(Q^2)$.

For reasons that will become clear shortly, we approximate $\rho_2(b)$ as another truncated series,

$$\rho_2(b) \approx \rho_{3\text{-pole}}(b) \sum_{n=0}^N \beta_n P_n^{(2)}(\Lambda^2 b^2/4), \quad (23)$$

where β_n are the expansion coefficients. After substituting this into Eq. (22), we get

$$F_2(Q^2) \approx \sum_{n=0}^N \beta_n B_n(Q^2/\Lambda^2), \quad (24)$$

where

$$B_0(y) = \frac{1}{(1+y)^3}, \quad (25)$$

$$B_1(y) = -\frac{\sqrt{3}y(y+5)}{\sqrt{5}(1+y)^5}, \quad (26)$$

$$B_2(y) = \frac{y^2(7y^2+64y+132)}{\sqrt{110}(1+y)^7}, \dots, \quad (27)$$

$$B_N(y) = \int_0^\infty P_N^{(2)}(x) w_2(x) J_0(2\sqrt{xy}) dx. \quad (28)$$

We set $\alpha_0 = \beta_0 = 1$ to ensure that $F_1(0) = F_2(0) = 1$. At high Q^2 , our parametrizations have the asymptotic behavior expected from the dimensional scaling laws [43]: $F_1 \propto (\Lambda/Q)^4$ and $F_2 \propto (\Lambda/Q)^6$. This justifies our choice of the series expansions for $\rho_1(b)$ and $\rho_2(b)$. Note that the terms A_0 and B_0 correspond to the dipole and “tripole” ($m = 3$) form factors (5). As shown in the next section, our parametrizations for F_1 and F_2 are flexible and efficiently fit experimental data.

Extraction of the proton radius. Based on the above results, we propose the following method for determining the proton charge radius. First, the measured cross sections are fit with the Rosenbluth formula [41] assuming the parametrizations (17) and (24) for the Dirac and Pauli form factors, where Λ , $\alpha_1, \dots, \alpha_N$, and β_1, \dots, β_N are $2N+1$ free parameters. Then the mean-square transverse charge radius $\langle b_1^2 \rangle$ is calculated from Λ and α_1 using Eq. (16). Finally, the proton radius is given by Eq. (10). Note that our method does not require measuring the form factor slope at $Q^2 = 0$ and considers the data at all Q^2 values. It also allows one to extract the transverse densities $\rho_1(b)$ and $\rho_2(b)$ given by Eqs. (15) and (23).

To illustrate our method, we apply it to the extensive and precise elastic electron-proton scattering data obtained by the A1 Collaboration at the Mainz Microtron MAMI [5, 6]. The collaboration measured 1422 cross sections at Q^2 values spanning the range from 0.004 to 1 GeV². Three magnetic spectrometers and six beam energies (180, 315, 450, 585, 720, and 855 MeV) were used, resulting in 18 distinct experimental data groups. To overcome the problem of achieving the absolute normalization of the measurement with sub-percent precision, they exploited the large redundancy of the data and introduced 31 free normalization parameters, fit simultaneously with the different form factor models. The A1 Collaboration obtained the following value for the proton charge radius:

$$r_E = 0.879(5)_{\text{stat}}(4)_{\text{syst}}(2)_{\text{model}}(4)_{\text{group}} \text{ fm}, \quad (29)$$

where the numbers in parentheses represent the statistical, systematic, model, and “group” uncertainties. The statistical uncertainty accounts for all point-to-point errors of the cross sections, not only those due to counting statistics. The “group” uncertainty was introduced because of an unexplained difference between the radii obtained using the spline and the polynomial groups of form factor models.

Following the original analysis [5, 6], we fit the data with our parametrizations by minimizing the objective function

$$\chi^2 = \sum_i \frac{(p_i \sigma_i^{\text{exp}} - \sigma_i^{\text{fit}})^2}{(p_i \Delta \sigma_i)^2}, \quad (30)$$

where σ_i^{exp} are the measured cross sections, $\Delta \sigma_i$ are their point-to-point uncertainties, σ_i^{fit} are the model cross sec-

TABLE I. Group-wise cross-validation results for different expansion orders before ($\lambda = 0$) and after ($\lambda > 0$) regularization was applied.

N	$\lambda = 0$		$\lambda > 0$		
	χ^2_{train}	χ^2_{test}	λ	χ^2_{train}	χ^2_{test}
1	4934	5114			
2	1949	2029			
3	1876	2358			
4	1854	2255			
5	1574	1682	0.02	1574	1657
6	1566	1703	0.07	1571	1664
7	1557	1912	0.2	1570	1672
8	1544	2060	0.4	1569	1679

tions [41], and p_i are known combinations of 31 free normalization parameters. The total number of fit parameters is $2N+32$, where N is the order of the form factor expansions (17) and (24). When choosing the value of N , it is important to avoid both underfitting and overfitting—a problem known as the bias-variance trade-off. The popular reduced chi-square test is not appropriate for this purpose because the number of degrees of freedom is ill-defined for a nonlinear fit [44]. Instead, we use cross-validation and regularization, which are standard techniques in statistical learning [45, 46].

Careful cross-validation is critical to finding the right balance in the bias-variance trade-off. Typically, a model is cross-validated by randomly dividing the data into k subsets, fitting the model to $k-1$ of them, testing it on the remaining subset, and repeating the last two steps k times so that each of the subsets is used as a test set exactly once. However, this procedure assumes that errors on the data points are uncorrelated. We instead perform cross-validation by holding out each of the 18 experimental data groups in turn and testing on that group while training on the others. Recall that the data groups correspond to different spectrometer and beam energy combinations. This 18-fold group cross-validation allows us to minimize overfitting to systematic artifacts by ensuring that the model generalizes well to unseen experimental conditions.

The cross-validation results for different orders N are shown in Table I, where χ^2_{train} and χ^2_{test} are the total chi-square values (30) obtained on the training and test sets, respectively. Note that each data point occurs only once in test sets but 17 times in training sets. For this reason, χ^2_{train} has been divided by 17 to make it directly comparable to χ^2_{test} . While χ^2_{train} monotonically decreases as N increases and the model becomes more flexible, χ^2_{test} reaches a minimum at $N = 5$. This indicates underfitting for $N < 5$ and overfitting for $N > 5$.

TABLE II. Objective function values and extracted radii for the regularized models trained on the full dataset.

N	λ	L	χ^2	$\langle b_1^2 \rangle$ (GeV $^{-2}$)	r_E (fm)
5	0.02	1584	1576	11.49	0.889
6	0.07	1580	1573	11.42	0.887
7	0.2	1579	1572	11.37	0.885
8	0.4	1578	1571	11.32	0.883

To control the overfitting in the higher-order models ($N \geq 5$), we add Tikhonov regularization to our objective function:

$$L = \chi^2 + \lambda \sum_{n=1}^N (\alpha_n^2 + \beta_n^2), \quad (31)$$

where α_n and β_n are the expansion coefficients and λ is the regularization parameter. The second term in Eq. (31) encourages the sum of the squares of the expansion coefficients to be small and thus reduces the flexibility of the model in a controlled way. We determine the optimal regularization parameter for each order by scanning a range of λ values and choosing the one that results in the lowest χ^2_{test} . One can see from Table I that regularization improves χ^2_{test} without significantly compromising χ^2_{train} . As expected, the optimal λ value and the improvement in χ^2_{test} increase with N .

After the optimal values of λ are determined, we train the $N \geq 5$ models on the full dataset (see Table II). We use the $N = 5$ model as our main fit and the higher orders to estimate model misspecification uncertainty. Note that we achieve a similar χ^2 value to that of Ref. [6] while using a more efficient parametrization of the form factors (1576 for 11 parameters vs. 1565 for 16 parameters). Our cross section normalizations differ from those determined in the original analysis by less than 0.3%.

The form factors and the transverse densities given by our main fit are shown in Fig. 1 with 68% confidence intervals. The point-to-point (statistical) uncertainties are determined by propagating the errors of the fit parameters taking into account the full covariance matrix. To estimate the systematic uncertainties, we follow the original analysis and refit our model using four modifications of the cross section data. These modifications correspond to the upper and lower bounds of (1) the energy cut in the elastic tail and (2) all other systematic effects linear in the scattering angle [6]. We perform all fits with floating normalizations and use the largest deviation from the primary fit as an uncertainty estimate. For further details on the data analysis, the reader is referred to Supplemental Material [41] and our Python code [47].

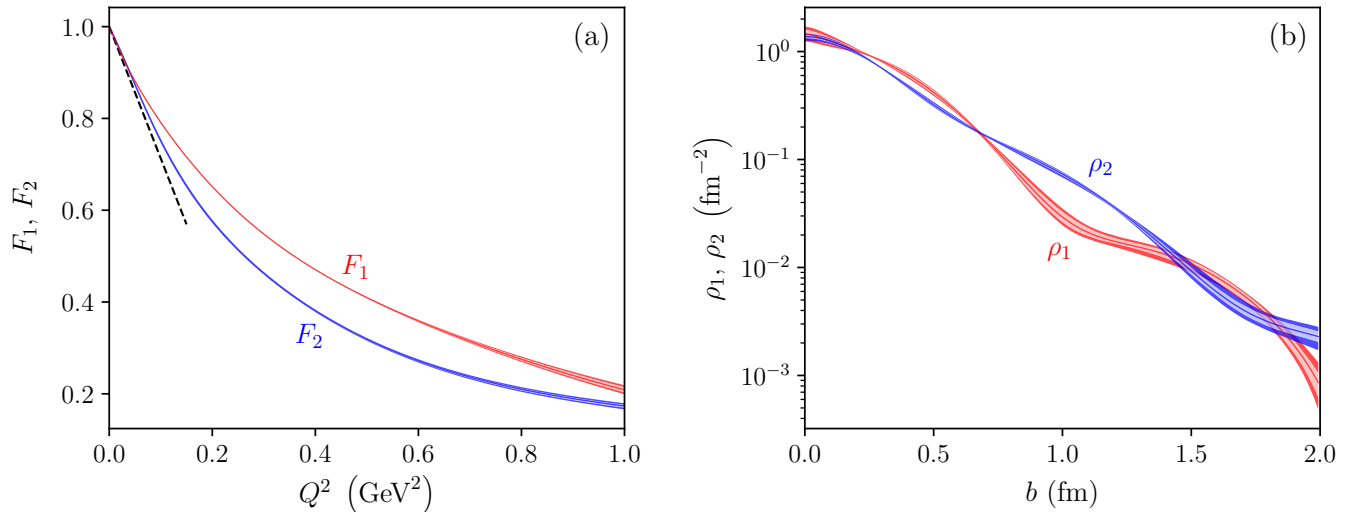


FIG. 1. Form factors and transverse densities extracted using our best model ($N = 5$, $\lambda = 0.02$). (a) Form factors F_1 (red) and F_2 (blue) as functions of Q^2 . The black dashed line is a tangent to F_1 at $Q^2 = 0$ corresponding to the mean-square transverse charge radius $\langle b_1^2 \rangle = 11.49 \text{ GeV}^{-2}$. Note that our extraction of $\langle b_1^2 \rangle$ is based on Eq. (8) rather than Eq. (9). (b) Transverse densities ρ_1 (red) and ρ_2 (blue) as functions of b . In both panels, lighter inner bands indicate the 68% statistical confidence intervals of the corresponding quantities, while darker outer bands show the 68% statistical and systematic confidence intervals added in quadrature.

Our final extraction of the proton charge radius from the full A1 data yields

$$r_E = 0.889(5)_{\text{stat}}(5)_{\text{syst}}(4)_{\text{model}} \text{ fm}, \quad (32)$$

where the model uncertainty is estimated based on the higher-order values of r_E listed in Table II. Our radius is larger by 0.01 fm than the original result (29), but both values are consistent given their uncertainties. Therefore, we confirm that the A1 data imply a large proton radius, although the possibility of unrecognized systematic errors can never be ruled out.

Conclusion. We have presented a novel method for extracting the proton charge radius from elastic scattering data that does not require determining the slope of G_E at $Q^2 = 0$. The method is based on Eq. (10) relating r_E to the second moment of the transverse charge density $\rho_1(b)$. This density is the two-dimensional Fourier transform of the Dirac form factor $F_1(Q^2)$ and has a proper relativistic interpretation. As a consequence, $\rho_1(b)$ and r_E can be determined by analyzing all available scattering data, not just those obtained at low Q^2 values. Another novelty is the use of F_1 instead of the usual G_E to extract the proton radius. To facilitate the analysis, we have proposed reasonable parametrizations not only for the form factors $F_1(Q^2)$ and $F_2(Q^2)$, but also for the transverse densities $\rho_1(b)$ and $\rho_2(b)$.

We have applied our method to the extensive data obtained by the A1 Collaboration [5, 6]. To find the right balance between underfitting and overfitting, we have used cross-validation and regularization—best practices from the field of statistical learning often overlooked in

nuclear physics. Figure 1 shows the form factors and the transverse densities that we have extracted. Our method has yielded the proton radius (32), which is consistent with the A1 value (29) but larger by 0.01 fm. Therefore, our reanalysis has confirmed that the full A1 data lead to the proton charge radius that contradicts the muonic hydrogen results [16, 17]. This means that the discrepancy cannot be explained by issues with data fitting and extrapolation. Further progress can be achieved by combining our approach with a careful reanalysis of all available electron-proton scattering data. Finally, the method can be extended to better understand other properties of the proton such as its magnetic radius and higher-order density moments.

We thank Prof. J. C. Bernauer for his comments that helped to improve the manuscript.

-
- [1] E. Rutherford, Collision of α particles with light atoms. IV. An anomalous effect in nitrogen, *Philos. Mag.* **37**, 581 (1919).
 - [2] R. Hofstadter and R. W. McAllister, Electron scattering from the proton, *Phys. Rev.* **98**, 217 (1955).
 - [3] R. Hofstadter, Electron scattering and nuclear structure, *Rev. Mod. Phys.* **28**, 214 (1956).
 - [4] G. G. Simon, Ch. Schmitt, F. Borkowski, and V. H. Walther, Absolute electron-proton cross sections at low momentum transfer measured with a high pressure gas target system, *Nucl. Phys. A* **333**, 381 (1980).
 - [5] J. C. Bernauer *et al.* (A1 Collaboration), High-precision determination of the electric and magnetic form factors

- of the proton, *Phys. Rev. Lett.* **105**, 242001 (2010).
- [6] J. C. Bernauer *et al.* (A1 Collaboration), Electric and magnetic form factors of the proton, *Phys. Rev. C* **90**, 015206 (2014).
 - [7] X. Zhan *et al.*, High-precision measurement of the proton elastic form factor ratio $\mu_p G_E/G_M$ at low Q^2 , *Phys. Lett. B* **705**, 59 (2011).
 - [8] M. Mihovilović *et al.*, First measurement of proton's charge form factor at very low Q^2 with initial state radiation, *Phys. Lett. B* **771**, 194 (2017).
 - [9] M. Mihovilović *et al.*, The proton charge radius extracted from the Initial State Radiation experiment at MAMI, [arXiv:1905.11182](https://arxiv.org/abs/1905.11182).
 - [10] W. Xiong *et al.*, A small proton charge radius from an electron-proton scattering experiment, *Nature* **575**, 147 (2019).
 - [11] P. J. Mohr, D. B. Newell, and B. N. Taylor, CODATA recommended values of the fundamental physical constants: 2014, *Rev. Mod. Phys.* **88**, 035009 (2016).
 - [12] A. Beyer *et al.*, The Rydberg constant and proton size from atomic hydrogen, *Science* **358**, 79 (2017).
 - [13] H. Fleurbaey, S. Galtier, S. Thomas, M. Bonnaud, L. Julien, F. Biraben, F. Nez, M. Abgrall, and J. Guéna, New measurement of the 1S-3S transition frequency of hydrogen: Contribution to the proton charge radius puzzle, *Phys. Rev. Lett.* **120**, 183001 (2018).
 - [14] N. Bezginov, T. Valdez, M. Horbatsch, A. Marsman, A. C. Vutha, and E. A. Hessels, A measurement of the atomic hydrogen Lamb shift and the proton charge radius, *Science* **365**, 1007 (2019).
 - [15] A. Grinin, A. Matveev, D. C. Yost, L. Maisenbacher, V. Wirthl, R. Pohl, T. W. Hänsch, and T. Udem, Two-photon frequency comb spectroscopy of atomic hydrogen, *Science* **370**, 1061 (2020).
 - [16] R. Pohl *et al.*, The size of the proton, *Nature* **466**, 213 (2010).
 - [17] A. Antognini *et al.*, Proton structure from the measurement of 2S-2P transition frequencies of muonic hydrogen, *Science* **339**, 417 (2013).
 - [18] R. Pohl, R. Gilman, G. A. Miller, and K. Pachucki, Muonic hydrogen and the proton radius puzzle, *Annu. Rev. Nucl. Part. Sci.* **63**, 175 (2013).
 - [19] C. E. Carlson, The proton radius puzzle, *Prog. Part. Nucl. Phys.* **82**, 59 (2015).
 - [20] J.-P. Karr, D. Marchand, and E. Voutier, The proton size, *Nat. Rev. Phys.* **2**, 601 (2020).
 - [21] V. B. Berestetskii, E. M. Lifshitz, and L. P. Pitaevskii, *Quantum Electrodynamics* (Pergamon Press, Oxford, 1982).
 - [22] F. Halzen and A. D. Martin, *Quarks and Leptons: An Introductory Course in Modern Particle Physics* (Wiley, New York, 1984).
 - [23] A. W. Thomas and W. Weise, *The Structure of the Nucleon* (Wiley-VCH, Berlin, 2001).
 - [24] G. A. Miller, Defining the proton radius: A unified treatment, *Phys. Rev. C* **99**, 035202 (2019).
 - [25] M. Vanderhaeghen and T. Walcher, Long range structure of the nucleon, *Nucl. Phys. News* **21**, 14 (2011).
 - [26] E. Kraus, K. E. Mesick, A. White, R. Gilman, and S. Strauch, Polynomial fits and the proton radius puzzle, *Phys. Rev. C* **90**, 045206 (2014).
 - [27] M. Horbatsch and E. A. Hessels, Evaluation of the strength of electron-proton scattering data for determining the proton charge radius, *Phys. Rev. C* **93**, 015204 (2016).
 - [28] I. Sick, Proton charge radius from electron scattering, *Atoms* **6**, 2 (2018).
 - [29] X. Yan, D. W. Higinbotham, D. Dutta, H. Gao, A. Gasparian, M. A. Khandaker, N. Liyanage, E. Pasyuk, C. Peng, and W. Xiong, Robust extraction of the proton charge radius from electron-proton scattering data, *Phys. Rev. C* **98**, 025204 (2018).
 - [30] F. Hagelstein and V. Pascalutsa, Lower bound on the proton charge radius from electron scattering data, *Phys. Lett. B* **797**, 134825 (2019).
 - [31] S. Pacetti and E. Tomasi-Gustafsson, Sensitivity of the elastic electron-proton cross section to the proton radius, *Eur. Phys. J. A* **56**, 74 (2020).
 - [32] Cl. Bouchiat, P. Fayet, and Ph. Meyer, Galilean invariance in the infinite momentum frame and the parton model, *Nucl. Phys. B* **34**, 157 (1971).
 - [33] M. Burkardt, Impact parameter dependent parton distributions and off-forward parton distributions for $\zeta \rightarrow 0$, *Phys. Rev. D* **62**, 071503(R) (2000).
 - [34] M. Burkardt, Impact parameter space interpretation for generalized parton distributions, *Int. J. Mod. Phys. A* **18**, 173 (2003).
 - [35] G. A. Miller, Charge densities of the neutron and proton, *Phys. Rev. Lett.* **99**, 112001 (2007).
 - [36] C. E. Carlson and M. Vanderhaeghen, Empirical transverse charge densities in the nucleon and the nucleon-to- Δ transition, *Phys. Rev. Lett.* **100**, 032004 (2008).
 - [37] G. A. Miller, Transverse charge densities, *Annu. Rev. Nucl. Part. Sci.* **60**, 1 (2010).
 - [38] S. Venkat, J. Arrington, G. A. Miller, and X. Zhan, Realistic transverse images of the proton charge and magnetization densities, *Phys. Rev. C* **83**, 015203 (2011).
 - [39] C. Lorcé, Charge distributions of moving nucleons, *Phys. Rev. Lett.* **125**, 232002 (2020).
 - [40] S. Yakubovich, Orthogonal polynomials with ultra-exponential weight functions: An explicit solution to the Ditkin–Prudnikov problem, *Constr. Approx.* **53**, 1 (2021).
 - [41] See Supplemental Material for additional information on the orthogonal polynomials $P_n^{(1)}$ and $P_n^{(2)}$, the rational functions A_n and B_n , the elastic scattering cross section, and the best-fit results obtained.
 - [42] G. A. Miller, E. Piasezky, and G. Ron, Proton electromagnetic-form-factor ratios at low Q^2 , *Phys. Rev. Lett.* **101**, 082002 (2008).
 - [43] S. J. Brodsky and G. R. Farrar, Scaling laws for large-momentum-transfer processes, *Phys. Rev. D* **11**, 1309 (1975).
 - [44] R. Andrae, T. Schulze-Hartung, and P. Melchior, Dos and don'ts of reduced chi-squared, [arXiv:1012.3754](https://arxiv.org/abs/1012.3754).
 - [45] Y. S. Abu-Mostafa, M. Magdon-Ismael, and H.-T. Lin, *Learning from Data: A Short Course* (AMLBook, 2012).
 - [46] G. James, D. Witten, T. Hastie, and R. Tibshirani, *An Introduction to Statistical Learning: With Applications in R* (Springer, New York, 2013).
 - [47] <https://github.com/gramolin/radius/>

Supplemental Material for “Transverse Charge Density and the Radius of the Proton”

FUNCTIONS $P_n^{(1)}$, $P_n^{(2)}$, A_n , AND B_n

Polynomials $P_n^{(\nu)}(x)$ are defined by the orthonormality condition given in Eq. (11) of the main text. The first six terms of $P_n^{(1)}(x)$ are

$$P_0^{(1)}(x) = 1, \quad (S1)$$

$$P_1^{(1)}(x) = \frac{x-2}{2\sqrt{2}}, \quad (S2)$$

$$P_2^{(1)}(x) = \frac{x^2 - 15x + 18}{6\sqrt{26}}, \quad (S3)$$

$$P_3^{(1)}(x) = \frac{13x^3 - 636x^2 + 5328x - 4896}{144\sqrt{4303}}, \quad (S4)$$

$$P_4^{(1)}(x) = \frac{331x^4 - 37620x^3 + 997200x^2 - 6105600x + 4708800}{224640\sqrt{1986}}, \quad (S5)$$

$$P_5^{(1)}(x) = \frac{676x^5 - 148095x^4 + 8964900x^3 - 169866000x^2 + 844128000x - 572702400}{1123200\sqrt{1375726}}. \quad (S6)$$

The first six polynomials $P_n^{(2)}(x)$ are

$$P_0^{(2)}(x) = 1, \quad (S7)$$

$$P_1^{(2)}(x) = \frac{x-3}{\sqrt{15}}, \quad (S8)$$

$$P_2^{(2)}(x) = \frac{5x^2 - 96x + 168}{24\sqrt{110}}, \quad (S9)$$

$$P_3^{(2)}(x) = \frac{11x^3 - 645x^2 + 6840x - 9000}{360\sqrt{1738}}, \quad (S10)$$

$$P_4^{(2)}(x) = \frac{79x^4 - 10368x^3 + 327420x^2 - 2517120x + 2743200}{1440\sqrt{11938638}}, \quad (S11)$$

$$P_5^{(2)}(x) = \frac{25187x^5 - 6219045x^4 + 433086780x^3 - 9730620900x^2 + 60331975200x - 57256264800}{151200\sqrt{541950039098}}. \quad (S12)$$

The rational functions $A_n(y)$ are defined by Eq. (21) in the main text. The first six terms are

$$A_0(y) = \frac{1}{(1+y)^2}, \quad (S13)$$

$$A_1(y) = -\frac{y(y+4)}{\sqrt{2}(1+y)^4}, \quad (S14)$$

$$A_2(y) = \frac{y^2(3y^2 + 22y + 39)}{\sqrt{26}(1+y)^6}, \quad (S15)$$

$$A_3(y) = -\frac{y^3(34y^3 + 352y^2 + 1187y + 1324)}{\sqrt{4303}(1+y)^8}, \quad (S16)$$

$$A_4(y) = \frac{y^4(1635y^4 + 21560y^3 + 104885y^2 + 225774y + 182520)}{78\sqrt{1986}(1+y)^{10}}, \quad (S17)$$

$$A_5(y) = -\frac{y^5(13257y^5 + 210730y^4 + 1324320y^3 + 4152432y^2 + 6528139y + 4127178)}{26\sqrt{1375726}(1+y)^{12}}. \quad (S18)$$

The rational functions $B_n(y)$ are defined by Eq. (28) in the main text. The first six terms are

$$B_0(y) = \frac{1}{(1+y)^3}, \quad (\text{S19})$$

$$B_1(y) = -\frac{\sqrt{3}y(y+5)}{\sqrt{5}(1+y)^5}, \quad (\text{S20})$$

$$B_2(y) = \frac{y^2(7y^2+64y+132)}{\sqrt{110}(1+y)^7}, \quad (\text{S21})$$

$$B_3(y) = -\frac{y^3(25y^3+321y^2+1260y+1580)}{\sqrt{1738}(1+y)^9}, \quad (\text{S22})$$

$$B_4(y) = \frac{\sqrt{3}y^4(635y^4+10324y^3+58410y^2+141476y+125935)}{\sqrt{3979546}(1+y)^{11}}, \quad (\text{S23})$$

$$B_5(y) = -\frac{y^5(378679y^5+7377979y^4+53840262y^3+189977062y^2+329168959y+225929067)}{\sqrt{541950039098}(1+y)^{13}}. \quad (\text{S24})$$

The first ten terms of $P_n^{(1)}$, $P_n^{(2)}$, A_n , and B_n can be calculated using the following Mathematica [S1] code:

```
$Assumptions = y > 0;
w[ν_] := 2*x^(ν/2)*BesselK[ν, 2*Sqrt[x]]/Gamma[ν+1]
P1 = Together[Orthogonalize[x^Range[0, 9], Integrate[#1**2*w[1], {x, 0, Infinity}]] &]]
P2 = Together[Orthogonalize[x^Range[0, 9], Integrate[#1**2*w[2], {x, 0, Infinity}]] &]]
A = Together[Integrate[#*w[1]*BesselJ[0, 2*Sqrt[x*y]], {x, 0, Infinity}] & /@ P1]
B = Together[Integrate[#*w[2]*BesselJ[0, 2*Sqrt[x*y]], {x, 0, Infinity}] & /@ P2]
```

ELASTIC SCATTERING CROSS SECTION

We use the beam energy, E , and the negative four-momentum transfer squared, Q^2 , as two independent kinematic variables. The electron scattering angle, θ , can be determined from E and Q^2 as

$$\theta = \arccos \left[1 - \frac{MQ^2}{E(2ME - Q^2)} \right]. \quad (\text{S25})$$

Also useful are the dimensionless kinematic variables τ and ε , defined as

$$\tau = \frac{Q^2}{4M^2}, \quad (\text{S26})$$

$$\varepsilon = \left[1 + 2(1 + \tau) \tan^2 \frac{\theta}{2} \right]^{-1}. \quad (\text{S27})$$

The differential cross section for unpolarized elastic electron-proton scattering is given by the Rosenbluth formula

$$\frac{d\sigma_0}{d\Omega} = \frac{\sigma_{\text{red}}}{\varepsilon(1 + \tau)} \frac{d\sigma_{\text{Mott}}}{d\Omega}, \quad (\text{S28})$$

where

$$\sigma_{\text{red}} = \varepsilon G_E^2(Q^2) + \tau G_M^2(Q^2) = \varepsilon [F_1(Q^2) - \tau \kappa F_2(Q^2)]^2 + \tau [F_1(Q^2) + \kappa F_2(Q^2)]^2 \quad (\text{S29})$$

is the so-called reduced cross section and $d\sigma_{\text{Mott}}/d\Omega$ is the Mott cross section describing the scattering of electrons on spinless point charged particles. The Sachs form factors G_E and G_M are often approximated as

$$G_E(Q^2) \approx G_{\text{dip}}(Q^2), \quad (\text{S30})$$

$$G_M(Q^2) \approx \mu G_{\text{dip}}(Q^2), \quad (\text{S31})$$

where

$$G_{\text{dip}}(Q^2) = \left(1 + \frac{Q^2}{0.71 \text{ GeV}^2}\right)^{-2} \quad (\text{S32})$$

is the standard dipole form factor and $\mu = 1 + \kappa$ is the magnetic moment of the proton. The corresponding reduced cross section is

$$\sigma_{\text{dip}} = (\varepsilon + \mu^2 \tau) G_{\text{dip}}^2(Q^2). \quad (\text{S33})$$

BEST-FIT RESULTS

Here we provide additional information on our best model ($N = 5$, $\lambda = 0.02$): the best-fit parameters in Table S1, the extracted electric and magnetic form factors in Fig. S1, and the raw cross section fits in Fig. S2. Note that all numerical results and plots presented in this Letter can be reproduced using our Python analysis code [S2]. The A1 Collaboration data that we use are publicly available as Supplemental Material of Ref. [S3].

TABLE S1. Expansion coefficients for our best fit. The scale parameter was found to be $\Lambda = 1.16 \pm 0.03 \text{ GeV}$.

	$n = 0$	$n = 1$	$n = 2$	$n = 3$	$n = 4$	$n = 5$
α_n	1	0.65 ± 0.06	1.85 ± 0.14	6.09 ± 0.58	9.8 ± 1.1	5.88 ± 0.77
β_n	1	-0.05 ± 0.07	-2.78 ± 0.23	-8.73 ± 0.62	-11.5 ± 0.8	-5.75 ± 0.42

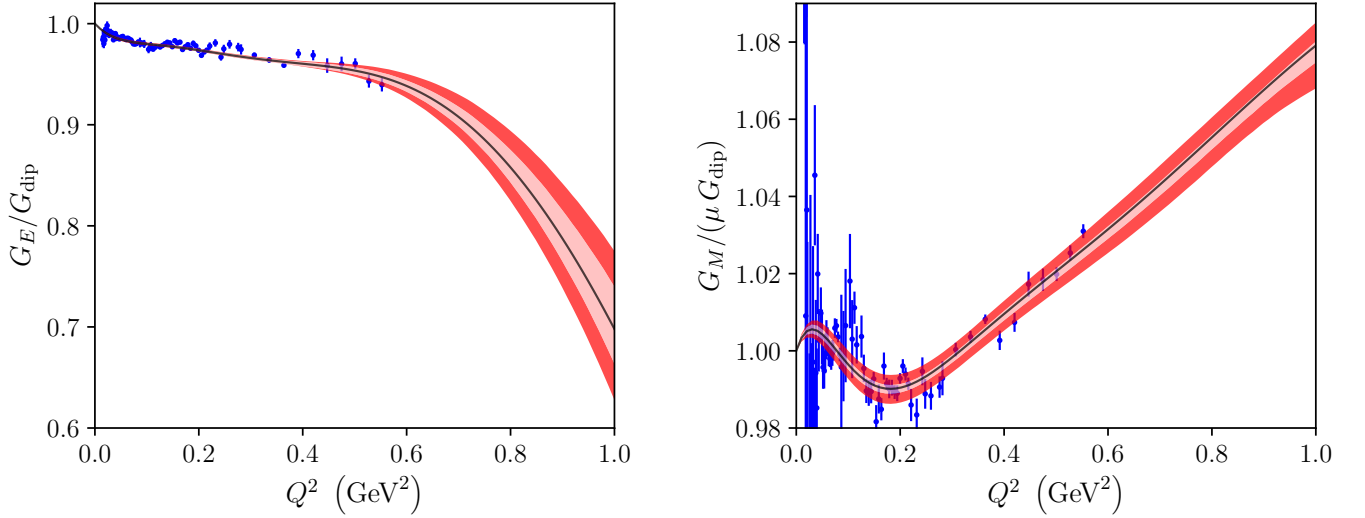


FIG. S1. Extracted electric (left panel) and magnetic (right panel) form factors as functions of Q^2 . We determine G_E and G_M from F_1 and F_2 using Eq. (1) of the main text and scale them by the corresponding dipole form factors, Eqs. (S30) and (S31). The lighter inner bands around the black best-fit lines are the 68% statistical confidence intervals, while the darker outer bands are the 68% statistical and systematic confidence intervals added in quadrature. We compare our extraction with the values of G_E and G_M obtained in Ref. [S3] using the Rosenbluth separation technique (blue data points with error bars representing statistical uncertainties). The Rosenbluth results are model-independent but based only on a subset of the cross section data.

[S1] Wolfram Research, Inc., Mathematica, Version 12.1, Champaign, IL (2021).

[S2] <https://github.com/gramolin/radius/>

[S3] J. C. Bernauer *et al.* (A1 Collaboration), Electric and magnetic form factors of the proton, *Phys. Rev. C* **90**, 015206 (2014).

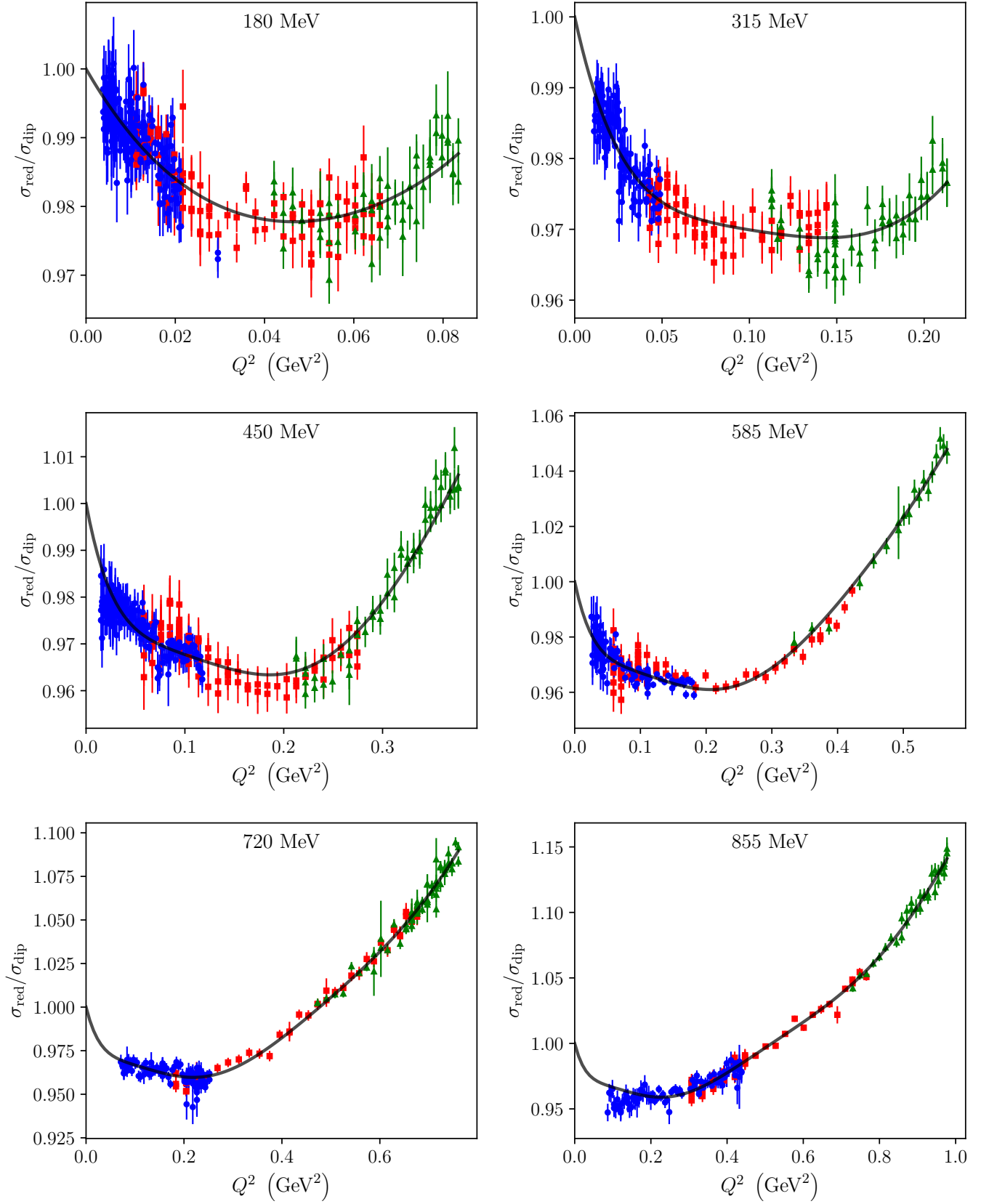


FIG. S2. Experimental data [S3] and our best fit as functions of Q^2 for six different beam energies (180, 315, 450, 585, 720, and 855 MeV). The data points are the measured reduced cross sections (S29) scaled by our best-fit normalizations and divided by the corresponding dipole cross sections (S33). Different markers represent different spectrometers: ■ A, ● B, and ▲ C. The error bars indicate point-to-point uncertainties of the cross section values.